How to cite: Angew. Chem. Int. Ed. 2023, e202307962
doi.org/10.1002/anie.202307962

Organic Solar Cells Hot Paper

Terminally Chlorinated and Thiophene-linked Acceptor-Donor-Acceptor Structured 3D Acceptors with Versatile Processability for High-efficiency Organic Solar Cells

Hongbin Chen, Bin Kan, Peiran Wang, Wanying Feng, Longyu Li, Shuchao Zhang, Tianqi Chen, Yang Yang, Tainan Duan, Zhaoyang Yao, Chenxi Li, Xiangjian Wan, and Yongsheng Chen**

Abstract: To exploit the potential of our newly developed three-dimensional (3D) dimerized acceptors, a series of chlorinated 3D acceptors (namely CH8-3/4/5) were reported by precisely tuning the position of chlorine (Cl) atom. The introduction of Cl atom in central unit affects the molecular conformation. Whereas, by replacing fluorinated terminal groups (CH8-3) with chlorinated terminal groups (CH8-4 and CH8-5), the red-shift absorption and enhanced crystallization are achieved. Benefiting from these, all devices received promising power conversion efficiencies (PCEs) over 16 % as well as decent thermal/photo-stabilities. Among them, PM6:CH8-4 based device yielded a best PCE of 17.58 %. Besides, the 3D merits with multi alkyl chains enable their versatile processability during the device preparation. Impressive PCEs of 17.27 % and 16.23 % could be achieved for non-halogen solvent processable devices prepared in glovebox and ambient, respectively. 2.88 cm^2 modules also obtained PCEs over 13 % via spin-coating and blade-coating methods, respectively. These results are among the best performance of dimerized acceptors. The decent performance of CH8-4 on small-area devices, modules and non-halogen solvent-processed devices highlights the versatile processing capability of our 3D acceptors, as well as their potential applications in the future.

Introduction

Solution-processed organic solar cells (OSCs) have been regarded as one of the transformative technologies which can convert sunlight to electricity under different circumstances including indoor or outer space.[1] In combination with its unique merits of flexibility and semi-transparency, OSCs have great potential in the application of Internet of Things (IoT) and wearable self-powered flexible devices.[1c,d] Over the last three decades, the OSCs have experienced great improvements and the power conversion efficiencies (PCEs) of OSCs have soared to more than 19 %,[1c,d,2] which shows great commercial potential of utilizing solar energy in the future. Particularly, the emerging of non-fullerene small-molecular acceptors (NFAs), such as ITIC,[3] F-series molecules[4] and Y6[5], provides an efficient approach to settle the dilemma of trade-off between open-circuit voltage (V_{oc}) and short-circuit current density (J_{sc}). Although remarkable progress in the PCEs has been achieved, the stability of OSCs remain a major issue that needs to be addressed urgently, which is also a prerequisite for the application of OSCs.[6]

Recently, some dimerized typed NFAs based on Y-series molecules come to the fore, exhibiting superior device stability and considerable PCE compared to other type NFAs.[6a,7] However, many dimerized NFAs is constructed by the end of end units with/out a connected unit, leading to half of end units were integrated in the resulted linear molecular skeleton instead of flanked in corresponding monomer.[6a,7a,b] Giving the crucial role of end units in

[*] H. Chen, B. Kan, T. Chen
School of Materials Science and Engineering, National Institute for Advanced Materials, Nankai University
Tianjin 300350 (China)
E-mail: kanbin04@nankai.edu.cn

H. Chen, P. Wang, W. Feng, L. Li, S. Zhang, Z. Yao, C. Li, X. Wan, Y. Chen
State Key Laboratory and Institute of Elemento-Organic Chemistry, The Centre of Nanoscale Science and Technology and Key Laboratory of Functional Polymer Materials, Renewable Energy Conversion and Storage Center (RECAST), College of Chemistry, Nankai University
Tianjin 300071 (China)
E-mail: yschen99@nankai.edu.cn

Y. Yang
The Institute of Seawater Desalination and Multipurpose Utilization, Ministry of Natural Resources (Tianjin)
Tianjin 300192 (China)

T. Duan
Chongqing Institute of Green and Intelligent Technology, Chongqing School, University of Chinese Academy of Sciences (UCAS Chongqing), Chinese Academy of Sciences (China)

molecule packing, the part-integrated end units might exert a reverse influence on the intermolecular interaction, which would hinder the further improvement of device performance of OSCs.[8] The dimerized NFAs tethered by alkyl side chains have been developed to solve above mentioned dilemma and the simultaneously enhanced efficiency/stability of polymer solar cells based on such dimerized acceptors has been demonstrated.[7f] To further solve this dilemma and exploit the full potential of dimerized NFAs, a new-type conjugated-skeleton connection mode assembled by central units of CH-series NFAs and thiophene unit with fluorination is developed in our latest work, extending conventionally linear molecular skeletons towards three-dimension (3D).[9] Most importantly, diverse potential advantages such as enhanced molecular packing, low reorganization energies, improved absorption coefficient in near infrared region and better stability have been verified due to its unleashed end units and greatly extended conjugated backbone.[10] Furthermore, the morphology stability of active layers based on such 3D acceptors with largely twisted molecular plane can be enhanced by forming a more robust packing network through not only the strong π–π stacking but also sufficient noncovalent interactions. [7g,7h] Benefiting from simultaneous fluorination on both central and end units, 3D NFA (CH8-1) displayed optimized film morphologies and charge transport behaviors, thus resulting a PCE of 17.0 %.[9a]

Compared to fluorination, chlorination of typical acceptor-donor-acceptor (A–D–A) NFAs can provide numerous merits,[11] such as enhanced crystallinity, improved optical absorption coefficient and light-harvesting range, and reduced energy loss due to the inherent difference in electronegativity and atom radius between fluorine and chlorine atom.[2b,12] It is also well-known that the increasing polarizability of halogen could enhance the magnitude of their σ-holes and consequently the strength of their respective intermolecular interactions,[13] thus improving charge transport and reducing charge recombination and even ameliorating the stability of corresponding OSC device.[14]

With those in mind, to further explore the potential of our newly developed 3D dimerized acceptors, a series of chlorinated acceptors with 3D configuration (namely CH8-3/4/5 in Figure 1a) were designed and synthesized by precisely tuning the position of Cl atom. Although the replacing of F atom with Cl atom on the central unit (CH8-4 vs. CH8-5) leads to a quite different dihedral angles between their two wings, but make little impact on the absorption and energy levels. Whereas, in comparison with CH8-3 with fluorinated terminal groups, both other two acceptors (CH8-4 and CH8-5) with chlorinated terminal groups displayed red-shifted absorptions and enhanced crystallinity. When blended with wide band gap polymer donor poly((4,8-bis(5-(2-ethylhexyl)-4-fluoro-2-thienyl)benzo[1,2-b:4,5-b′]dithiophene-2,6-diyl)-2,5-thiophenediyl(5,7-bis(2-ethylhexyl)-4,8-dioxo-4H,8H-benzo[1,2-c:4,5-c′]dithiophene-1,3-diyl)-2,5-thiophenediyl) (PM6), all the corresponding devices obtained PCEs over 16 % and decent thermal/photo-stabilities. Among them, PM6:CH8-4 based device yielded the best PCE of 17.58 % together with a high J_{sc} of 26.05 mA cm^{-2} and a fill-factor (*FF*) over 75 %. To further demonstrate its application potential, devices based on the blends of PM6:CH8-4

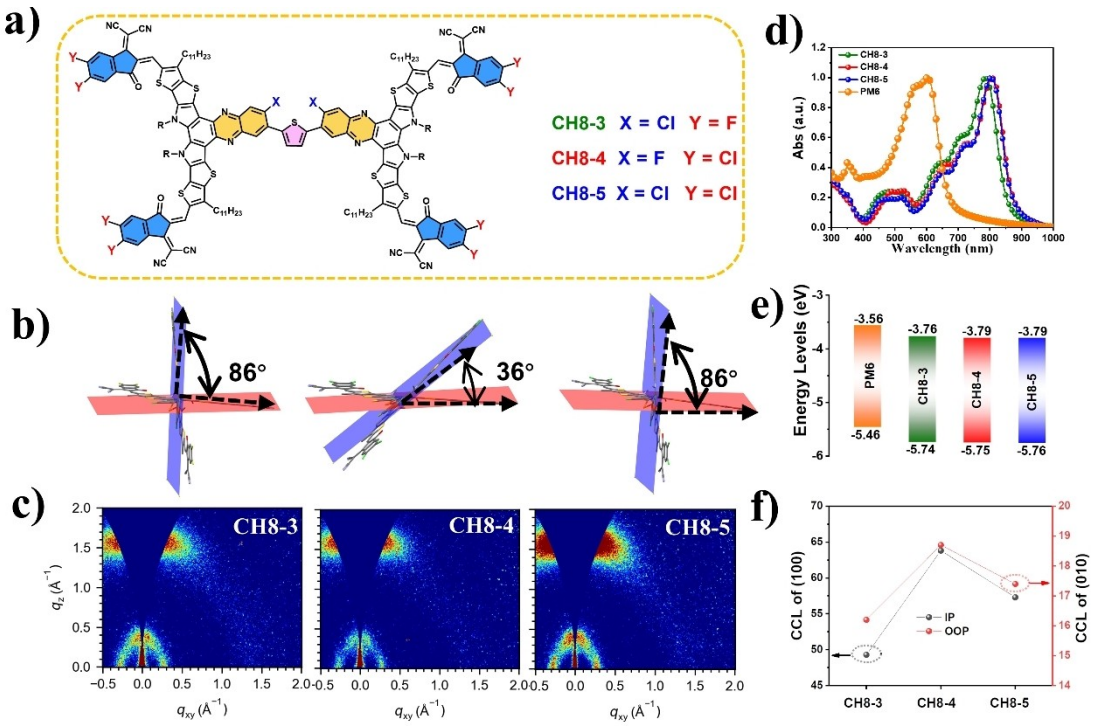

Figure 1. a) The chemical structures of CH8-3/4/5, respectively. b) The illustration of dihedral angle between two wings in CH8-3/4/5, respectively. c) GIWAXS images of CH8-3/4/5 based neat films, respectively. d) Normalized absorption profiles of CH8-3/4/5 together with PM6. e) The energy levels of PM6 and CH8-3/4/5. f) The coherence length of (100) in IP and (010) in OOP for CH8-3/4/5 based films.

with multiple processing capabilities were studied and achieved encouraging results, such as a PCE of 17.27 % for the non-halogen solvent (*o*-XY) processed devices. To our knowledge, these results are among the best performance of dimerized acceptors based binary devices.[6a,7] Meanwhile, 2.88 cm^2 solar cell modules received promising PCEs of 13.59 % and 13.27 % via spin-coating and blade-coating from its o-xylene solution, respectively. Our results highlight the promising development of such chlorinated 3D acceptors in fabricating efficient and process-insensitive OSCs.

Results and Discussion

The chemical structures of CH8-3/4/5 are displayed in Figure 1a, and the corresponding synthetic routes are presented as Scheme S1. Firstly, 4-bromo-5-fluorobenzene-1,2-diamine and 4-bromo-5-chlorobenzene-1,2-diamine with high active C–Br bond were selected as the raw materials to prepare the fused-ring intermediates according to our reported synthetic methods for CH-series molecules.[8] Immediately, the highly active C–Br bond provides an opportunity to carry out the Stille coupling reaction with 2,5-bis(trimethylstannyl)thiophene, which thusly afforded the four aldehyde substituted compounds. Lastly, 2-(5,6-difluoro-3-oxo-2,3-dihydro-1H-inden-1-ylidene)malononitrile (2F-IC) or 2-(5,6-dichloro-3-oxo-2,3-dihydro-1H-inden-1-ylidene)malononitrile (2Cl-IC) was used as the ending group to deliver target molecules CH8-3/4/5 via the four-fold Knoevenagel condensation reaction, respectively. Because of their 3D merits and multiple alkyl chains, the solubilities of CH8-3, CH8-4 and CH8-5 in chloroform at room temperature are measured to be 33, 28, and 17 mg/mL (Figure S1), respectively, enabling their solution-processable charterers. Besides, compared with CH8-5 with most Cl atom, CH8-3 and CH8-4 show better solubility in o-XY solvent (Figure S2).

Considering their structures, these acceptors are composed of two independent A–D–A structured wings[15] and the central thiophene linkers (Figure 1a).[9a] Based on the calculation results using the density functional theory (DFT) method, the dihedral angle between two wings of CH8-3 and CH8-5, in which have the Cl atom on the central extending unit, are much larger than that of CH8-4 (86° vs. 36°) due to the different interaction between F/Cl atom and S atom on linkage unit (Figure 1b). While, the halogen atoms on the ending groups have negligible impact on the spatial conformation of these acceptors. Afterward, their molecular packings in the solid state were studied by grazing incidence wide-angle X-ray scattering (GIWAXS) measurements.[16] The GIWAXS images are depicted in Figure 1c, and the line-cut profiles in in-plane (IP) and out-of-plane (OOP) directions are displayed in Figure S3. An obvious π-π diffraction peak (010) located in the OOP direction is observed for three neat films, suggesting that the CH8-3/4/5 adopted a preferred face-on molecular orientations. In comparison with CH8-3, both CH8-4 and CH8-5 exhibited longer coherence lengths (CL) of (010) and (100) orientations (Figure 1f), implying their better crystallinities caused by the chlorinated terminal groups. Among them, CH8-4 shows slightly reduced π-π stacking and alkyl-to-alkyl distances together with the largest coherence lengths (CLs) (Table S1), which can be attributed to its smallest dihedral angle and chlorinated terminal groups.

The absorption profiles of CH8-3/4/5 in dilute chloroform solutions and neat films were depicted in Figure S4 and Figure 1d, respectively. As listed in Table 1, the maximum absorption peak of CH8-3 in solution is located at 734 nm. Compared with CH8-3 whose ending unit is 2F-IC unit, CH8-4/5 featured with 2Cl-IC unit shows obvious red-shift absorption in solutions, consisting with the general trend observed in typical A–D–A small-molecular acceptors.[17] In neat films, these acceptors display similar absorption patterns in the range of 600–900 nm with absorption peaks of 786, 806 and 804 nm for CH8-3/4/5, respectively, which are ≈50 nm red-shifted in comparison with those of their solutions. Among them, CH8-4 with chlorinated terminal groups and F-substituted central extending unit displays the most red-shift absorption in both solution and film state, suggesting the variable impact of halogen atom on their optical properties. More importantly, in the neat films and blend films (Figure S5 and Table S2), both CH8-4 and CH8-5 display slightly higher absorption extinction coefficients than CH8-3, which are beneficial for utilizing photons in their absorption ranges.

The energy levels of three acceptors in solid state were studied by the cyclic voltammetry (CV) measurement under the same conditions, and their CV curves are displayed in Figure S6. The highest occupied molecular orbital (HOMO) and lowest unoccupied molecular orbital (LUMO) energy levels of CH8-3, which are estimated from the onset of oxidation peak and reduction peak, are −5.74 and −3.76 eV, respectively. As diagrammed in Figure 1e, when comparing CH8-3 and CH8-5, it can be found out that the Cl atom on terminal group would lower the HOMO and LUMO energy levels because of its strong electron inductive effect. As a contrast, replacing the Cl with F atom on the central position has little influence on the energy levels between CH8-5 and CH8-4, suggesting the central halogen atoms mainly affect the conformation of such type molecules. The tendency of variation in their energy levels is further verified by calculated HOMO and LUMO energy levels as summarized in Table 1. Besides, their HOMO and LUMO electron cloud mainly distribute in the A–D–A featured wings (Figure S7). Therefore, it can be concluded that the energy levels of CH8-3/4/5 are mainly determined by their independent wings.

Table 1: Optical properties and energy levels of CH8-3, CH8-4, and CH8-5.

Molecules	$\lambda_{max}^{sol.}$ [nm]	λ_{max}^{film} [nm]	$E_g^{opt.}$ [eV]	$LUMO^{cv}$ [eV]	$LUMO^{DFT}$ [eV]	$HOMO^{cv}$ [eV]	$HOMO^{DFT}$ [eV]
CH8-3	734	786	1.44	−3.76	−3.58	−5.74	−5.60
CH8-4	755	806	1.40	−3.79	−3.65	−5.75	−5.62
CH8-5	749	804	1.41	−3.79	−3.66	−5.76	−5.64

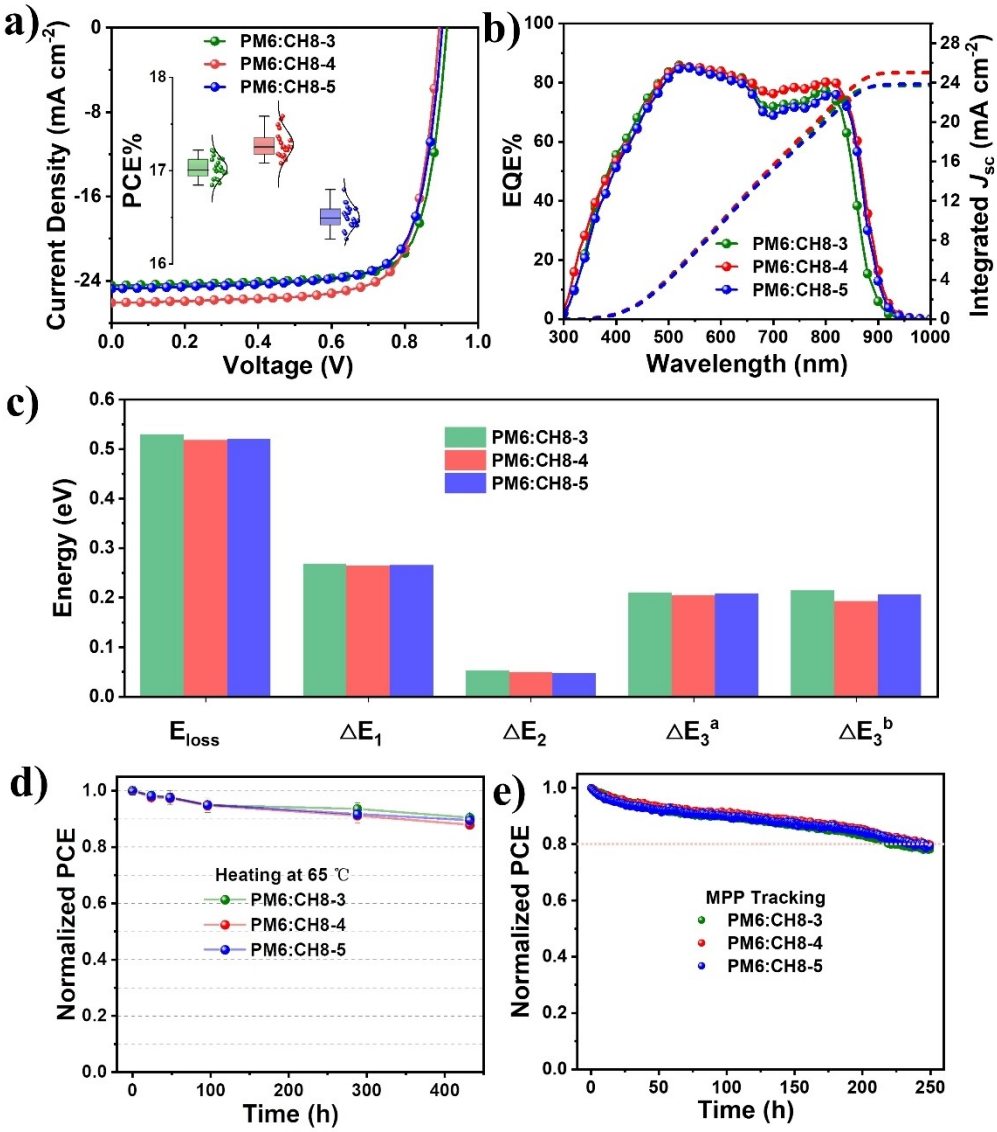

Figure 2. a) *J–V* curves of PM6:CH8-3/4/5 based optimized devices, and the inserted Figure shows the distribution of 20 devices. The active area of device was 4 mm^2. A shadow mask with an area of 0.324 mm^2 was used during the *J–V* testing. b) EQE curves and integrated J_{sc} curves of PM6:CH8-3/4/5 based devices, respectively. c) Energy losses of PM6:CH8-3/4/5, and ΔE_3^a is calculated from qV_{rad}^{oc}- qV^{oc}, ΔE_3^b is calculated from $-kT\ln(EQE_{EL})$. d) Thermal stability and e) photo-stability of three blends-based optimal devices.

The combination of polymer donor PM6 and CH8-3/4/5 provides a complementary absorption range covered from 300–900 nm and well-matched energy levels. To evaluate their photovoltaic performance, conventional devices were fabricated by using the architecture of indium tin oxide (ITO)/poly(3,4-ethylenedioxythiophene)-poly(styrenesulfonate) (PEDOT:PSS)/active layers/poly-((2,7-bis(2-ethylhexyl)-1,2,3,6,7,8-hexahydro-1,3,6,8-tetraoxobenzo[lmn][3,8]phenanthroline-4,9-diyl)-2,5-thiophenediyl(9,9-bis(3-(dimethylamino)propyl)-9H-fluorene-2,7-diyl)-2,5 thiophenediyl) (PNDIT-F3N)/Ag. After optimizing the weight ratio of donor and acceptor, the ratio of solvent additive, and post thermal-annealing treatment (Table S3–S5), all the devices exhibited over 16 % efficiencies along with satisfactory *FF*s over 75 %, demonstrating their potential in fabricating efficient OSCs. Figure 2a displays the current–voltage (*J–V*) curves of optimized devices using PM6:CH8-3, PM6:CH8-4 and PM6:CH8-5, respectively. Compared with CH8-3 and CH8-5 based devices, CH8-4 based device achieved a best PCE of 17.58 %. To our knowledge, this device performance represents one of the best for 3D acceptors (Table S6). As listed in Table 2, the differences in their PCEs are mainly due to their quite different J_{sc} values, which are 24.44, 26.05, and 24.75 mA cm^{-2}, respectively. The results were further verified by their integrated J_{sc} values of 23.69, 25.02 and 23.85 mA cm^{-2} for CH8-3, CH8-4, and CH8-5 based devices, respectively, which are within 4 % mismatch with their J_{sc} values from *J–V* tests. As shown in Figure 2b, the photoelectron response ranges of three devices follow the same

Table 2: Photovoltaic parameters of optimized devices. The average data in parentheses are calculated from the top best 20 devices.

BHJ	V_{oc} [V]	J_{sc} [mA cm^{-2}]	FF [%]	PCE [%]
PM6:CH8-3	0.915	24.44	77.0	17.22
	(0.911 ± 0.003)	(24.39 ± 0.21)	(76.6 ± 0.4)	(17.03 ± 0.11)
PM6:CH8-4	0.894	26.05	75.5	17.58
	(0.893 ± 0.004)	(25.83 ± 0.28)	(74.9 ± 0.4)	(17.29 ± 0.14)
PM6:CH8-5	0.902	24.75	75.2	16.79
	(0.896 ± 0.005)	(24.62 ± 0.17)	(74.8 ± 0.6)	(16.50 ± 0.12)

trend of their absorptions, in which CH8-4 and CH8-5 exhibited broader and red-shifted external quantum efficiencies (EQEs) response range in comparison with CH8-3. Meanwhile, the EQE values for PM6:CH8-4 based device are obviously higher in the range of 650–820 nm, corresponding to the contributions of CH8-4. These results suggest efficient photoelectric conversion process occurred in the PM6:CH8-4 based device (discussed below), leading to its highest J_{sc} value. As shown in Figure S8, all optimal devices displayed IQE values of 80–90 % in the range of 400–800 nm. While, there are still much room for further improving the IQE values of these optimal devices to the unit, and thus delivering better OSC performance.

To explain the variation of their V_{oc}s, a detailed energy loss (E_{loss}) analysis was conducted according to the detailed balance theory.[18] The optical band gaps (E_g) of PM6:CH8-3/4/5 blend films obtained from the derivatives of the EQE curves are 1.444, 1.412 and 1.417 eV (Figure S9), respectively.[18] The E_{loss} (estimated by the equation of $E_{loss} = E_g$ - qV_{oc}) of the corresponding devices are calculated to be 0.529, 0.515 and 0.520 eV, respectively. As shown in Figure 2c and Table S7, three optimized devices share almost the same radiative recombination energy losses above the band gap (ΔE_1). The radiative recombination energy losses below the band gap (ΔE_2) gradually decrease from 0.052 to 0.049 to 0.047 eV for CH8-3, CH8-4 and CH8-5 based devices. Meanwhile, PM6:CH8-4 based device yielded a smallest non-radiative recombination energy loss (ΔE_3) of 0.205 eV in three devices, which is further verified by the its larger electroluminescence quantum efficiency (EQE_{EL}) values (Figure S10). Please note the most concerned and suppressed ΔE_3 is a crucial contribution to the smallest E_{loss} for PM6:CH8-4 based device among three 3D dimerized acceptors, which also indicates a better trade-off between V_{oc} and J_{sc} to endow the maximized PCE for CH8-4 based OSCs.[19] Namely, the chlorinated terminal groups in our dimerized 3D acceptors would be beneficial for reducing the E_{loss} accompanied by an enhanced EQE_{EL}, which are consistent with the observed phenomenon in A–D–A featured SMAs and other type dimers.[20] While, the central Cl atom has negligible impact on the E_{loss}. Consequently, the PM6:CH8-4 based device could obtain a reasonable high V_{oc} of 0.894 V along with a promising J_{sc} over 26 mA cm^{-2}.

Apart from the PCEs, the stability of OSCs plays a vital role in future application,[21] and thus the thermal as well as photo stability of CH8-3/4/5-based devices were investigated following the reported conditions.[6a] As depicted in Figure 2d, under continuous heating at 65 °C in nitrogen-filled glovebox, all the optimized devices maintained ≈90 % of their initial efficiencies after thermal-aging for 430 h. In addition, under continuous 1 sun illumination simulated by light-emitting diode (LED) arrays using maximum power point (MPP) tracking mode, the PCEs of all devices slowly decreased without the dramatic burn-in degradation stage, and kept around 80 % of their original PCE after photo-aging for 250 h. Note that there is no obvious difference in the stability of CH8-3/4/5 based devices. Generally, the intermolecular π–π stacking and the weak noncovalent interactions in these 3D dimerized acceptors are beneficial for forming robust 3D packing network and thus stable morphological characteristics, which plays a vital role in realizing their good device stability despite the used conventional device structure.[9a] In comparison with conventional devices, inverted devices based on these dimeric acceptors achieved slightly lower PCEs (Figure S11 and Table S8), which are 15.88 %, 16.12 % and 15.53 % for PM6:CH8-3, PM6:CH8-4 and PM6:CH8-5, respectively. After thermal aging at 65 °C for 200 hours, all inverted devices could maintain over 95 % of their initial PCEs, further demonstrating the decent thermal stability of devices based on these 3D-acceptors.

To clarify the charge dynamic properties, such as charge generation and recombination behaviors in three optimized devices, the relationship between photocurrent density (J_{ph}) and effective voltage (V_{eff}) was conducted, and the results are shown in Figure 3a.[22] The probabilities of exciton dissociation, estimating by calculated the ratio of J_{sc} under short-circut condition and the saturation current density (J_{sat}), are as high as 0.97 for all three optimal devices, in agreement with their quite high photoluminescence (PL) quenching efficiencies in the blend films (Figure S12). The probability of charge collection, estimating by calculated the ratio of J_{sc} under maximum output condition and the J_{sat}, is 0.89 for PM6:CH8-4 based device, higher than those for other two devices (0.87), supporting the best J_{sc} value of CH8-4 based devices. The bimolecular recombination in all optimal devices was investigated by measuring the J_{sc} under different light density (P), whose relation can be expressed as $J_{sc} \propto P^S$. The resultant S values of all devices are in the range of 0.97–0.98 (Figure 3b), suggesting rather similar but little bimolecular recombination in these devices. By fitting the V_{oc} values versus light intensity ($V_{oc} \propto nkT/qP_{in}$) for corresponding optimal devices (Figure 3c), the slopes of PM6:CH8-3 and PM6:CH8-4 based devices are 1.10 kT/q, smaller than 1.15 kT/q of PM6:CH8-5 based device, indicating less trap-assisted recombination in PM6:CH8-3 and PM6:CH8-4 blends.

Subsequently, according to the space charge-limited current (SCLC) method, the charge carrier mobility in three optimal devices were estimated by fabricating the hole-only and electron-only devices, respectively. Figure S13 displays the corresponding curves, and Figure 3d shows the calculated charge mobilities, where the most balanced hole/electron mobilities ($3.66/3.47 \times 10^{-4}$ cm^2 V^{-1}s^{-1}) were received for PM6:CH8-3 based device, explaining its best FF of 77 %. Compared with CH8-3 based device, CH8-4/5 with

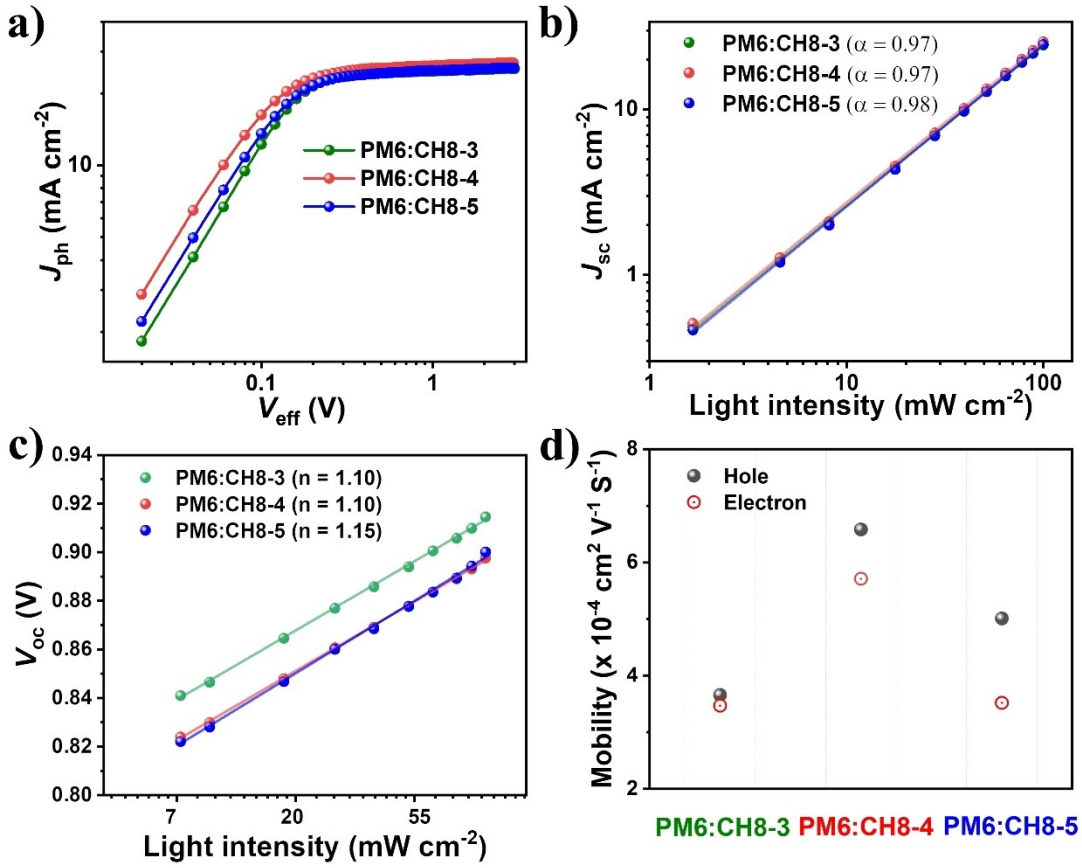

Figure 3. a) J_{ph} - V_{eff} curves, b) J_{sc} versus light intensity, c) V_{oc} versus light intensity, and d) hole and electron mobilities of PM6:CH8-3, PM6:CH8-4, and PM6:CH8-5 based optimal devices.

chlorinated terminal groups exhibited higher hole and electron mobilities, simultaneously, which can be correlated with their morphological characters as discussed below. The high and balanced hole/electron mobilities of 6.58/5.71 × 10^{-4} cm^2 $V^{-1}s^{-1}$ contribute the efficient charge transport process in PM6:CH8-4 device, resulting in its high J_{sc} and *FF* values.[23]

The different charge dynamic properties in CH8-3/4/5 based devices are partially determined by the morphologies of their blend films, which were revealed by atomic force microscopy (AFM) and GIWAXS measurements.[16,24] All blend films display appropriate phase separations and smooth surfaces with root-mean-square (RMS) roughness values from 1.03 nm of PM6:CH8-3 blend film to 1.71 nm of PM6:CH8-4 blend film (Figure S14). Distinctive morphologies with consecutive nanofiber networks in the blend films, which can be observed in AFM phase images (Figure 4a), are supposed to be one of the keys for their efficient charge transportation and extraction process. Besides, the fibril diameters are analyzed to be 8.4, 10.2 and 11.0 nm for CH8-3, CH8-4, and CH8-5 based films (Figure 4c and Figure S15), respectively. The slightly enhanced fibril diameters of the last two blend films can be ascribed to the improved crystallinity of CH8-4 and CH8-5, which has been revealed by GIWAXS results of their neat films. Overall, such fibrils with diameters around 10 nm provide effective pathways for exciton separation and charge generation in these 3D acceptor-based blend films.[2c,25]

Rather similar diffraction patterns were displayed in GIWAXS images (Figure 4b), which have an obvious π-π stacking peak (010) in OOP direction and alkyl-to-alkyl stacking peak (100) in both IP and OOP directions, indicating preferred face-on molecular orientations in three blend films. Their line-cut profiles in both directions are displayed as Figure 4d, and Scherer equation is used to estimate CLs of (010) in OOP and (100) in IP. The changes of CLs in the blend films follow the trend in their neat films as discussed above. As illustrated in Figure 4e, PM6:CH8-4 film obtained the largest CLs of π-π stacking (23.4 Å) and alkyl-to-alkyl stacking (67.5 Å), enabling their highest charge mobilities among them. To sum up, the chemical structures of these 3D acceptors play an important role in forming their different morphological features, which further affect their charge dynamic behaviors and the overall device performance. When blended with PM6, CH8-4 with chlorinated terminal groups and a small dihedral angle can form the optimal morphological characteristics, such as consecutive nanofibers with diameters of 10.2 nm, compact and ordered molecular packing in the blend film. All of these contribute the best performance of PM6:CH8-4 based device.

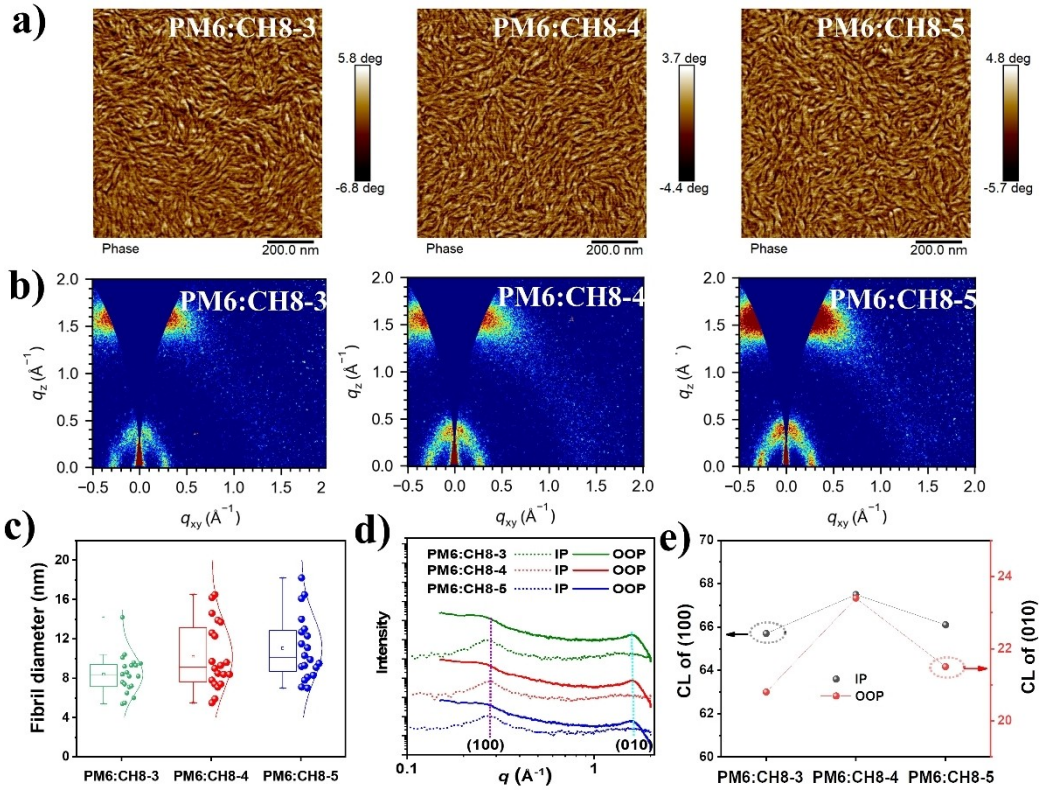

Figure 4. a) AFM phase images, and b) GIWAXS images of PM6:CH8-3/4/5 blend films, respectively. c) The distribution of the fibril width for PM6:CH8-3/4/5 blend films. d) Line-cut profiles in in-plane (IP) and out-of-plane (OOP) of GIWAXS. e) Coherence length of (100) in IP and (010) in OOP for PM6:CH8-3/4/5 blend films.

The excellent properties of these chlorinated 3D acceptors drive us to explore their practical potential under various processing conditions,[26] and PM6:CH8-4 was selected due to its superior performance. To avoid using halogen solvents, an eco-friendly and low-toxic non-halogen solvent xylene (*o*-XY) with high boiling point of 143–145 °C is adopted to dissolve the blend of PM6 and CH8-4.[27] First of all, absorption peaks of 741 and 831 nm were observed for CH8-4 in *o*-XY solution and its corresponding film, respectively (Figure S16 and Table S9). In comparison with its chloroform-prepared film, the *o*-XY-prepared neat film yields more red-shift absorption range, which is a favorable factor for achieving high-performance device. Figure 5a shows the *J*–*V* curves of devices prepared in glovebox and ambient condition from PM6:CH8-4 *o*-XY solution. During the fabrication of *o*-XY-processed device (Table S10), 2-Methoxynaphthalene (2-MN) which can be completely removed after thermal annealing was introduced as solid additive to tune the morphologies. Note that devices prepared in ambient means the active layer and interfacial layers are spin-coated outside the glovebox. It is encouraging that the *o*-XY-processed device exhibited a decent PCE of 17.27 %, comparable to that of the chloroform-processed device. Though the device prepared in ambient delivered a slightly lower PCE of 16.23 %, it still represents the top performance of air-processed OSCs.[28]

The morphologies of PM8:CH8-4 films prepared in glovebox and air were characterized by GIWAXS measurements. Figure 5b shows almost identical diffraction profiles for both films, which, combined with their quite similar molecular packing distances as well as the CLs of (010) and (100) (Figure 5c and Table S11), suggesting that the morphologies of PM6:CH8-4 films are less sensitive to preparation conditions. In our case, the performance of air-processed device is limited by its decreased *FF*, which might be mainly ascribed to its reduced charge collection efficiencies (0.82 for the device prepared in ambient vs. 0.88 for the device prepared in glovebox, Figure 5d), originating from the unfavorable interfacial contact between active layer and interfacial layers.

Based on above results, a module with an effective area of 2.88 cm^2, which composed of four sub-cells connected in series, was fabricated via spin-coating or blade-coating methods. The *J*–*V* curves of modules are presented in Figure 5e, and the corresponding parameters are summarized in Table 3. The resultant modules yielded over 13 % efficiencies, demonstrating the potential such-type acceptors in future applications.[26a] Note that efficiencies of 2.88 cm^2 module devices are lower than those of small-area devices. Generally, developing photovoltaic materials with high mobilities would benefit for preparing high-performance and thickness-insensitive OSCs, and further realizing efficient large-area devices.

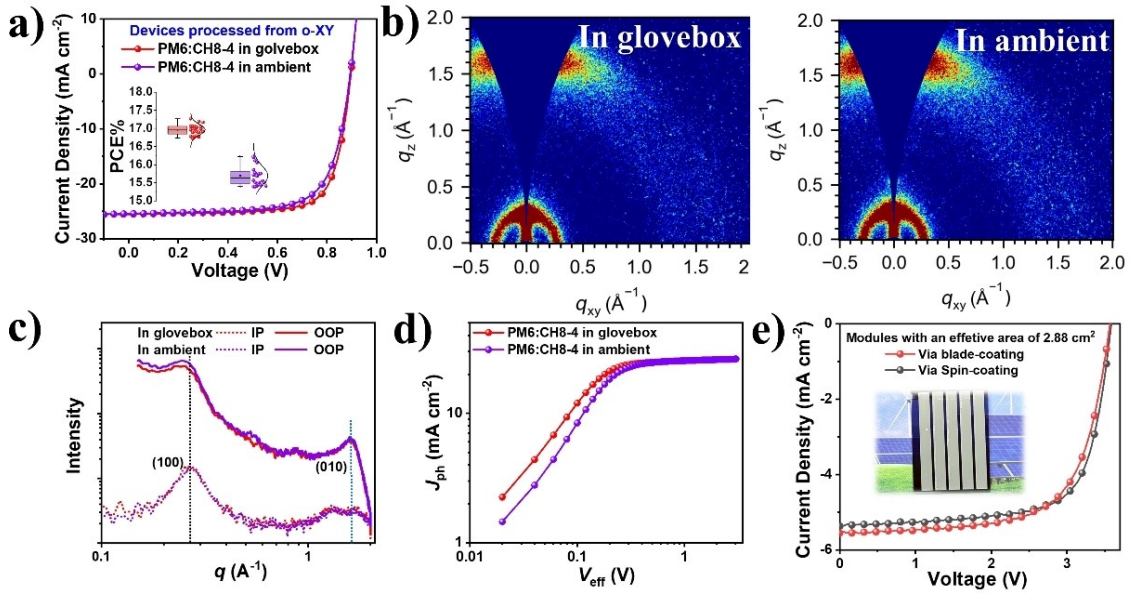

Figure 5. Devices prepared from PM6:CH8-4 xylene solutions. (a) *J–V* curves of devices fabricated in glovebox and ambient, and the inserted figure shows the distribution of best 20 devices. (b) GIWAXS images, and (c) the corresponding line-cut profiles in in-plane (IP) and out-of-plane (OOP) direction of PM6:CH8-4 blend films prepared in glovebox and ambient. (d) J_{ph} - V_{eff} curves of devices prepared in glovebox and ambient. (e) *J–V* curves of 2.88 cm^2 modules via spin-coating and blade-coating method.

Table 3: Photovoltaic parameters of devices prepared from PM6:CH8-4 xylene solutions.

BHJ	Device	V_{oc} [V]	J_{sc} [mA cm^{-2}]	*FF* [%]	PCE [%]
PM6:CH8-4	a	0.900	25.51	75.1	17.27
	b	0.894	25.40	71.4	16.23
	c	3.583	5.37	70.6	13.59
	d	3.567	5.56	67.0	13.27

[a] Device prepared in glovebox from o-XY solution. [b] Device prepared in ambient from o-XY solution; [c] 2.88 cm^2 module device prepared by spin-coating method; [d] 2.88 cm^2 module device prepared by blade-coating method.

Conclusion

In conclusion, a series of chlorinated 3D dimerized acceptors (namely CH8-3, CH8-4, and CH8-5) were reported to explore the effect of chlorination by precisely tuning the position and number of Cl atoms. The introduction of Cl atom in the central unit mainly affects the molecular conformation. Whereas, by replacing fluorinated terminal groups (CH8-3) with chlorinated terminal groups (CH8-4 and CH8-5), the red-shift absorption and enhanced crystallization could be achieved. Benefiting from their suitable energy levels and absorption abilities, all devices received promising PCEs over 16 % as well as decent thermal/photostabilities. Among them, PM6:CH8-4 based device yielded a best PCE of 17.58 % with a high J_{sc} of 26.05 mA cm^{-2}. In addition, impressive PCEs of 17.27 % and 16.23 % could be achieved for non-halogen solvent processable devices prepared in glovebox and ambient, respectively. Meanwhile, via spin-coating and blade-coating methods, 2.88 cm^2 modules obtained PCEs of 13.59 % and 13.27 %, respectively. As far as we know, CH8-4 represents the best design in dimerized 3D acceptors constructed through conjugation-extended phenazine central units, and the PCE record of 17.58 % is among the best performance of dimerized acceptors based binary devices. Their decent performances in small-area devices, solar cell modules, and non-halogen solvent processed devices highlight the versatile processability of these 3D-acceptors and their promising development for future applications.

Supporting Information

Detailed description of experimental methods, including molecular synthesis, device fabrication and characterization, additional data and Figures, and NMR spectra.

Acknowledgements

The authors gratefully acknowledge the financial support from NSFC (21935007, 52025033) and MoST (2022YFB4200400, 2019YFA0705900) of China, the 100 Young Academic Leaders Program of Nankai University (020-ZB22000110), the Fundamental Research Funds for the Central Universities, Nankai University (023-ZB22000105), and Haihe Laboratory of Sustainable Chemical Transformations.

Conflict of Interest

The authors declare no conflict of interest.

Data Availability Statement

The data that support the findings of this study are available in the supplementary material of this article.

Keywords: Chlorination · Non-Halogen Solvent · Organic Solar Cells · Three-Dimension Acceptors · Versatile Processability

[1] a) A. J. Gillett, A. Privitera, R. Dilmurat, A. Karki, D. Qian, A. Pershin, G. Londi, W. K. Myers, J. Lee, J. Yuan, S.-J. Ko, M. K. Riede, F. Gao, G. C. Bazan, A. Rao, T.-Q. Nguyen, D. Beljonne, R. H. Friend, *Nature* **2021**, *597*, 666–671; b) L. Meng, Y. Zhang, X. Wan, C. Li, X. Zhang, Y. Wang, X. Ke, Z. Xiao, L. Ding, R. Xia, H.-L. Yip, Y. Cao, Y. Chen, *Science* **2018**, *361*, 1094–1098; c) Y. Liu, B. Liu, C.-Q. Ma, F. Huang, G. Feng, H. Chen, J. Hou, L. Yan, Q. Wei, Q. Luo, Q. Bao, W. Ma, W. Liu, W. Li, X. Wan, X. Hu, Y. Han, Y. Li, Y. Zhou, Y. Zou, Y. Chen, Y. Li, Y. Chen, Z. Tang, Z. Hu, Z.-G. Zhang, Z. Bo, *Sci. China Chem.* **2022**, *65*, 224–268; d) Y. Liu, B. Liu, C.-Q. Ma, F. Huang, G. Feng, H. Chen, J. Hou, L. Yan, Q. Wei, Q. Luo, Q. Bao, W. Ma, W. Liu, W. Li, X. Wan, X. Hu, Y. Han, Y. Li, Y. Zhou, Y. Zou, Y. Chen, Y. Liu, L. Meng, Y. Li, Y. Chen, Z. Tang, Z. Hu, Z.-G. Zhang, Z. Bo, *Sci. China Chem.* **2022**, *65*, 1457–1497.

[2] a) K. Jiang, J. Zhang, C. Zhong, F. R. Lin, F. Qi, Q. Li, Z. Peng, W. Kaminsky, S.-H. Jang, J. Yu, X. Deng, H. Hu, D. Shen, F. Gao, H. Ade, M. Xiao, C. Zhang, A. K. Y. Jen, *Nat. Energy* **2022**, *7*, 1076–1086; b) Y. Cui, Y. Xu, H. Yao, P. Bi, L. Hong, J. Zhang, Y. Zu, T. Zhang, J. Qin, J. Ren, Z. Chen, C. He, X. Hao, Z. Wei, J. Hou, *Adv. Mater.* **2021**, *33*, 2102420; c) L. Zhu, M. Zhang, J. Xu, C. Li, J. Yan, G. Zhou, W. Zhong, T. Hao, J. Song, X. Xue, Z. Zhou, R. Zeng, H. Zhu, C.-C. Chen, R. C. I. MacKenzie, Y. Zou, J. Nelson, Y. Zhang, Y. Sun, F. Liu, *Nat. Mater.* **2022**, *21*, 656–663; d) G. Zhang, F. R. Lin, F. Qi, T. Heumüller, A. Distler, H.-J. Egelhaaf, N. Li, P. C. Y. Chow, C. J. Brabec, A. K. Y. Jen, H.-L. Yip, *Chem. Rev.* **2022**, *122*, 14180–14274; e) C. W. Tang, *Appl. Phys. Lett.* **1986**, *48*, 183–185.

[3] Y. Lin, J. Wang, Z.-G. Zhang, H. Bai, Y. Li, D. Zhu, X. Zhan, *Adv. Mater.* **2015**, *27*, 1170–1174.

[4] N. Qiu, H. Zhang, X. Wan, C. Li, X. Ke, H. Feng, B. Kan, H. Zhang, Q. Zhang, Y. Lu, Y. Chen, *Adv. Mater.* **2017**, *29*, 1604964.

[5] a) J. Yuan, Y. Zhang, L. Zhou, G. Zhang, H.-L. Yip, T.-K. Lau, X. Lu, C. Zhu, H. Peng, P. A. Johnson, M. Leclerc, Y. Cao, J. Ulanski, Y. Li, Y. Zou, *Joule* **2019**, *3*, 1140–1151; b) A. Karki, J. Vollbrecht, A. L. Dixon, N. Schopp, M. Schrock, G. N. M. Reddy, T.-Q. Nguyen, *Adv. Mater.* **2019**, *31*, 1903868; c) B. R. Luginbuhl, P. Raval, T. Pawlak, Z. Du, T. Wang, G. Kupgan, N. Schopp, S. Chae, S. Yoon, A. Yi, H. Jung Kim, V. Coropceanu, J.-L. Brédas, T.-Q. Nguyen, G. N. M. Reddy, *Adv. Mater.* **2022**, *34*, 2105943.

[6] a) Y. Liang, D. Zhang, Z. Wu, T. Jia, L. Lüer, H. Tang, L. Hong, J. Zhang, K. Zhang, C. J. Brabec, N. Li, F. Huang, *Nat. Energy* **2022**, *7*, 1180–1190; b) B. Fan, W. Gao, X. Wu, X. Xia, Y. Wu, F. R. Lin, Q. Fan, X. Lu, W. J. Li, W. Ma, A. K. Y. Jen, *Nat. Commun.* **2022**, *13*, 5946.

[7] a) H. Zhuo, X. Li, J. Zhang, S. Qin, J. Guo, R. Zhou, X. Jiang, X. Wu, Z. Chen, J. Li, L. Meng, Y. Li, *Angew. Chem. Int. Ed.* **2023**, *62*, e202303551; b) F. Qi, Y. Li, R. Zhang, F. R. Lin, K. Liu, Q. Fan, A. K. Y. Jen, *Angew. Chem. Int. Ed.* **2023**, *62*, e202303066; c) C. Sun, J.-W. Lee, C. Lee, D. Lee, S. Cho, S.-K. Kwon, B. J. Kim, Y.-H. Kim, *Joule* **2023**, *7*, 416–430; d) Z. Li, Z. Zhang, H. Chen, Y. Zhang, Y.-Q.-Q. Yi, Z. Liang, B. Zhao, M. Li, C. Li, Z. Yao, X. Wan, B. Kan, Y. Chen, *Adv. Energy Mater.* **2023**, *13*, 2300301; e) L. Zhang, Z. Zhang, D. Deng, H. Zhou, J. Zhang, Z. Wei, *Adv. Sci.* **2022**, *9*, 2202513; f) S. Li, R. Zhang, M. Zhang, J. Yao, Z. Peng, Q. Chen, C. Zhang, B. Chang, Y. Bai, H. Fu, Y. Ouyang, C. Zhang, J. A. Steele, T. Alshahrani, M. B. J. Roeffaers, E. Solano, L. Meng, F. Gao, Y. Li, Z.-G. Zhang, *Adv. Mater.* **2023**, *35*, 2206563; g) D. Meng, J. L. Yang, C. Xiao, R. Wang, X. Xing, O. Kocak, G. Aydin, I. Yavuz, S. Nuryyeva, L. Zhang, G. Liu, Z. Li, S. Yuan, Z.-K. Wang, W. Wei, Z. Wang, K. N. Houk, Y. Yang, *Proc. Natl. Acad. Sci. USA* **2020**, *117*, 20397–20403; h) D. Meng, R. Wang, J. B. Lin, J. L. Yang, S. Nuryyeva, Y.-C. Lin, S. Yuan, Z.-K. Wang, E. Zhang, C. Xiao, D. Zhu, L. Jiang, Y. Zhao, Z. Li, C. Zhu, K. N. Houk, Y. Yang, *Adv. Mater.* **2021**, *33*, 2006120.

[8] H. Chen, Y. Zou, H. Liang, T. He, X. Xu, Y. Zhang, Z. Ma, J. Wang, M. Zhang, Q. Li, C. Li, G. Long, X. Wan, Z. Yao, Y. Chen, *Sci. China Chem.* **2022**, *65*, 1362–1373.

[9] a) H. Chen, Z. Zhang, P. Wang, Y. Zhang, K. Ma, Y. Lin, T. Duan, T. He, Z. Ma, G. Long, C. Li, B. Kan, Z. Yao, X. Wan, Y. Chen, *Energy Environ. Sci.* **2023**, *16*, 1773–1782; b) H. Chen, X. Cao, X. Xu, C. Li, X. Wan, Z. Yao, Y. Chen, *Chin. J. Polym. Sci.* **2022**, *40*, 921–927.

[10] X. Meng, M. Li, K. Jin, L. Zhang, J. Sun, W. Zhang, C. Yi, J. Yang, F. Hao, G.-W. Wang, Z. Xiao, L. Ding, *Angew. Chem. Int. Ed.* **2022**, *61*, e202207762.

[11] a) H. Chen, T. Zhao, L. Li, P. Tan, H. Lai, Y. Zhu, X. Lai, L. Han, N. Zheng, L. Guo, F. He, *Adv. Mater.* **2021**, *33*, 2102778; b) H. Wang, F. He, *Synlett* **2021**, *32*, 1297–1302; c) Z. Luo, R. Ma, J. Yu, H. Liu, T. Liu, F. Ni, J. Hu, Y. Zou, A. Zeng, C.-J. Su, U. S. Jeng, X. Lu, F. Gao, C. Yang, H. Yan, *Nat. Sci. Rev.* **2022**, *9*, nwac076.

[12] Y. Cui, H. Yao, J. Zhang, K. Xian, T. Zhang, L. Hong, Y. Wang, Y. Xu, K. Ma, C. An, C. He, Z. Wei, F. Gao, J. Hou, *Adv. Mater.* **2020**, *32*, 1908205.

[13] V. V. Panikkattu, A. Tran, A. S. Sinha, E. W. Reinheimer, E. B. Guidez, C. B. Aakeröy, *Cryst. Growth Des.* **2021**, *21*, 7168–7178.

[14] Q. Yang, H. Chen, J. Lv, P. Huang, D. Han, W. Deng, K. Sun, M. Kumar, S. Chung, K. Cho, D. Hu, H. Dong, L. Shao, F. Zhao, Z. Xiao, Z. Kan, S. Lu, *Adv. Sci.* **2023**, *10*, 2207678.

[15] X. Wan, C. Li, M. Zhang, Y. Chen, *Chem. Soc. Rev.* **2020**, *49*, 2828–2842.

[16] P. Müller-Buschbaum, *Adv. Mater.* **2014**, *26*, 7692–7709.

[17] G. Li, X. Zhang, L. O. Jones, J. M. Alzola, S. Mukherjee, L.-w. Feng, W. Zhu, C. L. Stern, W. Huang, J. Yu, V. K. Sangwan, D. M. DeLongchamp, K. L. Kohlstedt, M. R. Wasielewski, M. C. Hersam, G. C. Schatz, A. Facchetti, T. J. Marks, *J. Am. Chem. Soc.* **2021**, *143*, 6123–6139.

[18] a) Y. Wang, D. Qian, Y. Cui, H. Zhang, J. Hou, K. Vandewal, T. Kirchartz, F. Gao, *Adv. Energy Mater.* **2018**, *8*, 1801352; b) J. Liu, S. Chen, D. Qian, B. Gautam, G. Yang, J. Zhao, J. Bergqvist, F. Zhang, W. Ma, H. Ade, O. Inganäs, K. Gundogdu, F. Gao, H. Yan, *Nat. Energy* **2016**, *1*, 16089.

[19] S. Liu, J. Yuan, W. Deng, M. Luo, Y. Xie, Q. Liang, Y. Zou, Z. He, H. Wu, Y. Cao, *Nat. Photonics* **2020**, *14*, 300–305.

[20] C. Li, J. Zhou, J. Song, J. Xu, H. Zhang, X. Zhang, J. Guo, L. Zhu, D. Wei, G. Han, J. Min, Y. Zhang, Z. Xie, Y. Yi, H. Yan, F. Gao, F. Liu, Y. Sun, *Nat. Energy* **2021**, *6*, 605–613.

[21] a) Y. Qin, N. Balar, Z. Peng, A. Gadisa, I. Angunawela, A. Bagui, S. Kashani, J. Hou, H. Ade, *Joule* **2021**, *5*, 2129–2147; b) Y. Bai, Z. Zhang, Q. Zhou, H. Geng, Q. Chen, S. Kim, R. Zhang, C. Zhang, B. Chang, S. Li, H. Fu, L. Xue, H. Wang, W. Li, W. Chen, M. Gao, L. Ye, Y. Zhou, Y. Ouyang, C. Zhang, F. Gao, C. Yang, Y. Li, Z.-G. Zhang, *Nat. Commun.* **2023**, *14*, 2926.

[22] a) A. K. K. Kyaw, D. H. Wang, V. Gupta, W. L. Leong, L. Ke, G. C. Bazan, A. J. Heeger, *ACS Nano* **2013**, *7*, 4569–4577;

b) L. J. A. Koster, V. D. Mihailetchi, R. Ramaker, P. W. M. Blom, *Appl. Phys. Lett.* **2005**, *86*, 123509.
[23] X. Zhang, C. Li, J. Xu, R. Wang, J. Song, H. Zhang, Y. Li, Y.-N. Jing, S. Li, G. Wu, J. Zhou, X. Li, Y. Zhang, X. Li, J. Zhang, C. Zhang, H. Zhou, Y. Sun, Y. Zhang, *Joule* **2022**, *6*, 444–457.
[24] Y. Huang, E. J. Kramer, A. J. Heeger, G. C. Bazan, *Chem. Rev.* **2014**, *114*, 7006–7043.
[25] Q. Liu, Y. Jiang, K. Jin, J. Qin, J. Xu, W. Li, J. Xiong, J. Liu, Z. Xiao, K. Sun, S. Yang, X. Zhang, L. Ding, *Sci. Bull.* **2020**, *65*, 272–275.
[26] a) Y. Liu, J. Zhang, C. Tian, Y. Shen, T. Wang, H. Zhang, C. He, D. Qiu, Y. Shi, Z. Wei, *Adv. Funct. Mater.* **2023**, 2300778; b) J. Wan, L. Zeng, X. Liao, Z. Chen, S. Liu, P. Zhu, H. Zhu, Y. Chen, *Adv. Funct. Mater.* **2022**, *32*, 2107567; c) B. Fan, L. Ying, P. Zhu, F. Pan, F. Liu, J. Chen, F. Huang, Y. Cao, *Adv. Mater.* **2017**, *29*, 1703906.
[27] B. Liu, H. Sun, J.-W. Lee, J. Yang, J. Wang, Y. Li, B. Li, M. Xu, Q. Liao, W. Zhang, D. Han, L. Niu, H. Meng, B. J. Kim, X. Guo, *Energy Environ. Sci.* **2021**, *14*, 4499–4507.
[28] a) P. Li, M. Mainville, Y. Zhang, M. Leclerc, B. Sun, R. Izquierdo, D. Ma, *Small* **2019**, *15*, 1804671; b) H. Tang, J. Lv, K. Liu, Z. Ren, H. T. Chandran, J. Huang, Y. Zhang, H. Xia, J. I. Khan, D. Hu, C. Yan, J. Oh, S. Chen, S. Chu, P. W. K. Fong, H. Chen, Z. Xiao, C. Yang, Z. Kan, F. Laquai, S. Lu, G. Li, *Mater. Today* **2022**, *55*, 46–55.

Manuscript received: June 7, 2023
Accepted manuscript online: August 7, 2023
Version of record online: ■■, ■■

Research Articles

Organic Solar Cells

H. Chen, B. Kan,* P. Wang, W. Feng, L. Li, S. Zhang, T. Chen, Y. Yang, T. Duan, Z. Yao, C. Li, X. Wan, Y. Chen* e202307962

Terminally Chlorinated and Thiophene-linked Acceptor-Donor-Acceptor Structured 3D Acceptors with Versatile Processability for High-efficiency Organic Solar Cells

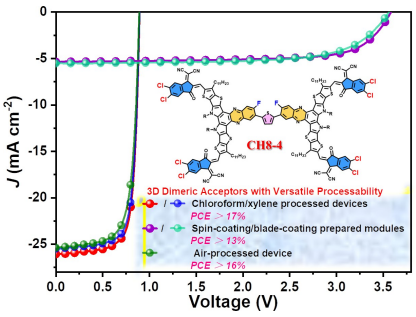

A series of terminally chlorinated and thiophene-linked three-dimensional (3D) dimerized acceptors were reported to explore the effect of chlorination by precisely tuning the position and number of chlorine atoms. The decent performance of PM6:CH8-4 on small-area devices, non-halogen solvent and air-processed devices, and 2.88 cm^2 solar cell modules highlights the versatile processing capability of our 3D acceptors.